



Cite this: RSC Adv., 2018, 8, 3858

## Synthesis of $\text{CrO}_x/\text{C}$ catalysts for low temperature $\text{NH}_3\text{-SCR}$ with enhanced regeneration ability in the presence of $\text{SO}_2$ †

Shuohan Yu,<sup>ab</sup> Sheng Xu,<sup>c</sup> Bowen Sun,<sup>ab</sup> Yiyang Lu,<sup>ab</sup> Lulu Li,<sup>ab</sup> Weixin Zou,<sup>ab</sup> Peng Wang,<sup>c</sup> Fei Gao,<sup>ID \*ab</sup> Changjin Tang<sup>ab</sup> and Lin Dong<sup>ID \*ab</sup>

Chromium oxide nano-particles with an average diameter of 3 nm covered by amorphous carbon ( $\text{CrO}_x/\text{C}$ ) were successfully synthesized. The synthesized  $\text{CrO}_x/\text{C}$  materials were used for the selective catalytic reduction of  $\text{NO}_x$  by  $\text{NH}_3$  ( $\text{NH}_3\text{-SCR}$ ), which shows superb  $\text{NH}_3\text{-SCR}$  activity and in particular, satisfactory regeneration ability in the presence of  $\text{SO}_2$  compared with Mn-based catalysts. The as-prepared catalysts were characterized by XRD, HRTEM, Raman, FTIR, BET, TPD, TPR, XPS and *in situ* FTIR techniques. The results indicated presence of certain amounts of unstable lattice oxygen exposed on the surface of  $\text{CrO}_x$  nano-particles with an average size of 3 nm in the  $\text{CrO}_x/\text{C}$  samples, which led to NO being conveniently oxidized to  $\text{NO}_2$ . The formed  $\text{NO}_2$  participated in  $\text{NH}_3\text{-SCR}$  activity, reacting with catalysts via a "fast  $\text{NH}_3\text{-SCR}$ " pathway, which enhanced the  $\text{NH}_3\text{-SCR}$  performance of the  $\text{CrO}_x/\text{C}$  catalysts. Furthermore, the stable lattice of the  $\text{CrO}_x$  species made the catalyst immune to the sulfation process, which was inferred to be the cause of its superior regeneration ability in the presence of  $\text{SO}_2$ . This study provides a simple way to synthesize stable  $\text{CrO}_x$  nano-particles with active oxygen, and sheds light on designing  $\text{NH}_3\text{-SCR}$  catalysts with highly efficient low temperature activity,  $\text{SO}_2$  tolerance, and regeneration ability.

Received 31st August 2017  
 Accepted 22nd December 2017

DOI: 10.1039/c7ra09680a  
[rsc.li/rsc-advances](http://rsc.li/rsc-advances)

## 1. Introduction

Low-temperature  $\text{NH}_3\text{-SCR}$  (<200 °C), which can be located downstream of electrostatic precipitators and even desulfurizers, where most of  $\text{SO}_2$  and dust have been removed, has been paid increasing attention in the past few decades.<sup>1–4</sup> Various transition metal oxides exhibit satisfactory activity for low-temperature  $\text{NH}_3\text{-SCR}$ , such as Mn, Fe, Cu, and Co.<sup>2,5–9</sup> Among them, Mn-based catalysts have become a focus for their excellent low-temperature activity and inherent environment-friendly nature.<sup>4,10–12</sup> According to literature, Mn-based catalysts have a unique advantage for low-temperature SCR (<200 °C) in contrast with other competitors. For example,

Hu *et al.* reported a Co–Mn/TiO<sub>2</sub> catalyst with superior  $\text{NH}_3\text{-SCR}$  activity at 200 °C.<sup>11</sup> Mn–Ce–Ti mix-oxide catalysts were recorded to exhibit an operating temperature window from 150 °C to 200 °C.<sup>12</sup> We also reported Mn–Fe–Ti mix-oxide catalysts with satisfactory  $\text{NH}_3\text{-SCR}$  activity from 100 °C to 350 °C.<sup>5</sup> However, the poor  $\text{SO}_2$  resistance performance of Mn-based catalysts limits their practical application.

According to the previous reports,<sup>4,13–15</sup> the tolerance of metal oxide based catalysts to  $\text{SO}_2$  depends on the type and oxidation state of the deposited metal, the nature of the support, and the type of reducing agent. In general, the rapid deactivation of  $\text{NH}_3\text{-SCR}$  catalysts involves two main mechanisms. One is the formation of ammonium salts.<sup>14,16–22</sup> The  $\text{SO}_2$  in the feed gas can be oxidized to  $\text{SO}_3$  on the surface of the catalysts, and the formed  $\text{SO}_3$  would respond to  $\text{NH}_3$  and water in feed gas transforming to  $\text{NH}_4\text{HSO}_4$ . The formed  $\text{NH}_4\text{HSO}_4$  would deposit on the surface of the catalysts, cover active sites, block pores of the catalysts, and result in the deactivation of the catalysts. The other fact is the irreversible sulfation of the active phase.<sup>14,16,18–23</sup> For most transition metal oxides usually reported as  $\text{NH}_3\text{-SCR}$  catalysts, such as Mn, Fe, Cu, and Co, all sulfating processes are spontaneous according to their Gibbs free energy values (Table S1†). In the sulfation process, formation of a metal sulfate requires breaking the metal oxide lattice. It is reasonable to predict that the more stable the metal oxides, the more difficult it is to break the metal oxide lattice and thus, harder is the sulfation of metal oxide. In general, the metal oxide with a high melting point has

<sup>a</sup>Key Laboratory of Mesoscopic Chemistry of MOE, School of Chemistry and Chemical Engineering, Nanjing University, Nanjing 210093, PR China. E-mail: donglin@nju.edu.cn; gaofei@nju.edu.cn

<sup>b</sup>Jiangsu Key Laboratory of Vehicle Emissions Control, Center of Modern Analysis, Nanjing University, Nanjing 210093, PR China

<sup>c</sup>National Laboratory of Solid State Microstructures, College of Engineering and Applied Sciences, Collaborative Innovation Center of Advanced Microstructures, Nanjing University, Nanjing 210093, China

† Electronic supplementary information (ESI) available: Band energy calculation, thermochemical data, band energy data, mass of metal sulfate formed on catalysts, surface atomic concentration of  $\text{SO}_2$  poisoned  $\text{CrO}_x/\text{C-450}$  sample, extra  $\text{NH}_3\text{-SCR}$  and water tolerance tests, XRD patterns, FTIR data, Raman data, extra TEM image,  $\text{NH}_3\text{-TPD}$  data,  $\text{H}_2\text{-TPR}$  data,  $\text{O}_2\text{-TPD}$  data, extra XPS spectra. See DOI: 10.1039/c7ra09680a



a stable crystal lattice. Thus, the melting point can be an indicator of the stability of the crystal lattice of metal oxides.<sup>24</sup> In the case of Mn-based catalysts,  $\text{MnO}_2$  has a low melting point (Table S1†), indicating its unstable structure, which is the cause of the severe irreversible sulfation of  $\text{MnO}_2$  in the  $\text{NH}_3$ -SCR process, particularly in the low temperature range ( $<200$  °C).<sup>13,14,25–28</sup>  $\text{Cr}_2\text{O}_3$ , which has the highest melting point among the transition metal oxides with  $\text{NH}_3$ -SCR activity (listed in Table S1†), was expected to have resistance to the sulfation process. Although the low  $\text{NH}_3$ -SCR activity of crystalline  $\text{Cr}_2\text{O}_3$  is unsatisfactory, amorphous  $\text{Cr}_2\text{O}_3$  exhibits superb low temperature  $\text{NH}_3$ -SCR activity, according to literature.<sup>29–33</sup> Thus, it appears to be a promising strategy to design a SCR catalyst with both low temperature activity and  $\text{SO}_2$  tolerance *via* enhancing the catalytic activity of crystalline  $\text{Cr}_2\text{O}_3$ .

Compared with traditional metal oxide catalysts with a large particle size, nano-sized catalysts often have significant amounts of unsaturated-coordinated atoms exposed on their surfaces. Unsaturated-coordinated atoms are usually active; thus, nano-sized catalysts exhibit unique redox ability and enhanced catalytic activity.<sup>34–36</sup> Therefore, decreasing the size of catalysts appears to be a promising strategy to enhance low temperature  $\text{NH}_3$ -SCR performance of crystalline  $\text{Cr}_2\text{O}_3$ . However, nano-particle materials have the disadvantage of instability and tend to aggregate due to their high surface energy and their abundant surface unsaturated atoms. Recently, metal oxide nano-particles catalysts derived from MOFs material were reported.<sup>37–39</sup> Through a thermal decomposition process under controlled atmosphere, MOFs built from metal ions or nodes and polyfunctional organic ligands can transform into nano-materials, including nano-particles, single atoms, and metal oxide clusters. Wu *et al.*<sup>40</sup> synthesized Co nano-particles and single atoms from Co MOF and Co/Zn bimetallic MOF. Similar results were also reported by Li *et al.*<sup>37</sup> and Sun's group.<sup>41</sup> The carbon from the organic ligands of MOFs remains in materials and can protect metal oxide nano-particles from aggregation.

Herein, novel  $\text{CrO}_x$  nano-particles covered by amorphous carbon ( $\text{CrO}_x/\text{C}$ ) have been synthesized by a MOFs assisted process for low temperature  $\text{NH}_3$ -SCR. MIL-101, with a metal node of 3 Cr atoms,<sup>42,43</sup> was employed as a precursor. The results of the catalytic tests for  $\text{NH}_3$ -SCR showed that the prepared  $\text{CrO}_x$  catalyst exhibited satisfactory activity and superior regeneration ability. According to a series of characterizations, the  $\text{CrO}_x/\text{C}$  catalyst was observed to be composed of  $\text{CrO}_x$  nano-particles with an eskolaite phase and activated lattice oxygen. It was deduced that the activated lattice oxygen was closely related to the enhanced  $\text{NH}_3$ -SCR activity of the  $\text{CrO}_x/\text{C}$  catalyst. The stable lattice of the eskolaite phase- $\text{CrO}_x$  inhibited the sulfating process, thus causing the  $\text{SO}_2$  tolerance and regeneration ability. To the best of our knowledge, it is the first time that a non-Mn catalyst with excellent low temperature  $\text{NH}_3$ -SCR activity and remarkable regeneration ability has been reported. This study provides a simple route to synthesize stable  $\text{CrO}_x$  nano-particles with active oxygen and shed light on designing low temperature  $\text{NH}_3$ -SCR catalysts with  $\text{SO}_2$  tolerance and regeneration ability.

## 2. Experimental details

### 2.1. Preparation of catalysts

Typically, MIL-101(Cr) was prepared by reacting terephthalic acid (332 mg, 2.0 mmol) with  $\text{Cr}(\text{NO}_3)_3 \cdot 9\text{H}_2\text{O}$  (800 mg, 2.0 mmol) and de-ionized water (9.5 mL) at 220 °C for 8 h. Microcrystalline green powders of MIL-101(Cr) were produced during the reaction. The obtained powders were washed by ammonium hydroxide, water, and ethanol, in sequence, 3 times each. The powders were dried and calcined at a certain temperature for 4 h under  $\text{N}_2$  flow, and the heating rate was set at 1 °C min<sup>−1</sup>. Finally, the cooled sample was exposed to air and denoted as  $\text{Cr}_2\text{O}_3/\text{C-X}$ , in which  $X$  represents the calcining temperature.

As reported in ref. 44, a  $\text{Cr}_2\text{O}_3$  sample was obtained by calcining  $\text{Cr}(\text{NO}_3)_3 \cdot 9\text{H}_2\text{O}$  at 450 °C for 4 h.  $\text{MnO}_2$  was purchased from Aladdin and was used without further purification. An active carbon supported  $\text{Cr}_2\text{O}_3$  catalyst was synthesized through a wetness impregnation process. Active carbon (1.00 g) was dispersed into de-ionized water (50 mL) containing  $\text{Cr}(\text{NO}_3)_3 \cdot 9\text{H}_2\text{O}$  (9.92 g). The turbid solution was oil-bath heated at 110 °C until the water was totally evaporated. The dried powders were calcined at 450 °C for 4 h under a  $\text{N}_2$  flow and the obtained sample was noted as  $\text{Cr}_2\text{O}_3/\text{C-WI}$ .

### 2.2. Characterizations

The X-ray diffraction (XRD) patterns of the catalysts were studied using an XRD-6000 X-ray diffractometer (Shimadzu). X-ray fluorescence (XRF) analysis was performed on an ARL-900 X-ray fluorescence analyzer. FTIR analysis was carried out using a NEXUS870 spectrometer (NICOLET, America). Raman spectra were measured at a resolution of <1 cm<sup>−1</sup> using a JY Labram HR 800 spectrophotometer equipped with an argon-ion laser source and an air-cooled CCD detector.  $\text{N}_2$  adsorption/desorption isotherms of the catalysts were obtained at −196 °C using an ASAP2020 physical adsorption instrument (Micromeritics) to calculate the BET surface area of the catalysts. TEM analysis was performed on a double-aberration corrected Titan™ cubed G2 60-300 S/TEM equipped with Super-X™ technology. X-ray energy dispersive spectroscopy (EDS) mappings were acquired using the Super-X EDS system, which is composed of four silicon drift detectors covering 0.7 s rad collection.

$\text{NH}_3$ -temperature programmed desorption ( $\text{NH}_3$ -TPD) experiments were performed using a multifunction chemisorption analyzer, equipped with a thermal conductivity detector (TCD). Samples were pretreated under a  $\text{NH}_3$ - $\text{N}_2$  flow ( $\text{NH}_3$  1%) at 150 °C for 1 h and were heated under  $\text{N}_2$  flow; the heating rate was set at 10 °C min<sup>−1</sup>.

$\text{O}_2$ -temperature programmed desorption ( $\text{O}_2$ -TPD) experiments were performed using a multifunction chemisorption analyzer, equipped with a thermal conductivity detector (TCD). Samples were pretreated under  $\text{O}_2$ -He flow ( $\text{O}_2$  25%) at 25 °C for 1 h and were heated under a He flow; the heating rate was set at 10 °C min<sup>−1</sup>.

$\text{H}_2$ -temperature programmed reduction ( $\text{H}_2$ -TPR) of the catalysts was recorded using a chemisorption analyzer. Samples were pretreated under a  $\text{N}_2$  flow at 200 °C for 1 h, and were



heated under a H<sub>2</sub>-Ar flow (H<sub>2</sub>, 7%); the heating rate was set at 10 °C min<sup>-1</sup>.

X-ray photoelectron spectroscopy (XPS) measurements were performed using a PHI 5000 VersaProbe spectrophotometer. The contents of the metal ions were measured *via* an inductive coupled plasma emission spectrometer (Optima 5300DV, PE). Energy referencing was accomplished by setting the adventitious carbon peak to 284.6 eV. The *ex situ* XPS details are described below. The sample was treated under a certain atmosphere for a certain time in a reaction chamber connected with the intro chamber of the XPS instrument. Following this, the reaction chamber was vacuumized and the treated sample was transferred to the XPS instrument without exposure to air.

The *in situ* DRIFT experiments were performed on a Nicolet Nexus 5700 FTIR spectrometer using a diffuse reflectance attachment (HARRICK) equipped with a reaction cell (ZnSe windows). The number of scans was 32 at a resolution of 4 cm<sup>-1</sup> and the spectra were presented as Kubelka-Munk function, referred to the background spectra of the recorded catalyst in N<sub>2</sub>.

### 2.3. NO oxidation tests

The NO oxidation tests were performed in a fixed-bed reactor with 0.2 g catalyst. The feed gas contained 500 ppm NO and 5 vol% O<sub>2</sub> with N<sub>2</sub> as the balance gas. The total flow rate of the feed gas was 100 mL min<sup>-1</sup>, corresponding to a space velocity of approximately 30 000 h<sup>-1</sup>. Including NO and NO<sub>2</sub>, the effluent gases were continuously analyzed at 150 °C by an online Thermo Fisher IS10 FTIR spectrometer equipped with a 2 m path-length gas cell (250 mL volume).

### 2.4. NH<sub>3</sub>-SCR activity, SO<sub>2</sub> poisoning, and regeneration tests

The NH<sub>3</sub>-SCR activity tests were performed in a fixed-bed reactor with 0.2 g catalyst. The feed gas contained 500 ppm NO, 500 ppm NH<sub>3</sub>, 5 vol% O<sub>2</sub>, 50 ppm SO<sub>2</sub> (when used), 5 vol% H<sub>2</sub>O (when used) and N<sub>2</sub> as the balance gas. The total flow rate of the feed gas was 100 mL min<sup>-1</sup>, corresponding to a space velocity of approximately 30 000 h<sup>-1</sup>. SO<sub>2</sub> poisoning and regeneration tests of catalysts were carried out at 150 °C. Including NO, NH<sub>3</sub>, NO<sub>2</sub>, and N<sub>2</sub>O, the effluent gases were continuously analyzed at 150 °C using an online Thermo Fisher IS10 FTIR spectrometer equipped with a 2 m path-length gas cell (250 mL volume).

### 2.5. Regeneration of SO<sub>2</sub> poisoned catalysts

SO<sub>2</sub> poisoned catalysts were regenerated at 300 °C for 30 min, and then were cooled down to room temperature. All the heat treatments were carried out under N<sub>2</sub> atmosphere.

The sulfating of metal oxide catalysts during SO<sub>2</sub> poisoning was investigated by inductively coupled plasma-emission spectroscopy (ICP).

The SO<sub>2</sub>-poisoned catalyst (0.2 g) was washed with deionized water for 5 times. The eluate was collected and diluted to 50 mL. The diluted eluate was investigated by ICP analysis. The contents of metal sulfate  $m_{\text{MSO}_4}$  were calculated using the equation below.

$$m_{\text{MSO}_4} = \frac{m_{\text{M}^{n+}} \times 0.05L \times M_{\text{MSO}_4}}{M_{\text{M}}}$$

where,  $m_{\text{M}^{n+}}$  is the content of the metal ion,  $M_{\text{MSO}_4}$  was obtained *via* ICP analysis and  $M_{\text{M}}$  is the molar mass of metal sulfate, which also corresponds to the molar mass of the metal ion.

For Cr oxide,  $m_{\text{Cr}_2(\text{SO}_4)_3} = m_{\text{Cr}^{3+}} \times 0.188$

For Mn oxide,  $m_{\text{MnSO}_4} = m_{\text{Mn}^{2+}} \times 0.137$

## 3. Results and discussion

### 3.1. NH<sub>3</sub>-SCR performance, SO<sub>2</sub> tolerance, and regeneration

The NH<sub>3</sub>-SCR activities of the CrO<sub>x</sub> samples derived from various precursors and MnO<sub>2</sub> are shown in Fig. 1 and S1†. As it was anticipated, all the catalysts derived from MIL-101 exhibited superior activities than pure Cr<sub>2</sub>O<sub>3</sub>. Remarkably, CrO<sub>x</sub>/C-450, parallel to MnO<sub>2</sub>, exhibited a wide operation temperature window from 125 °C to 200 °C. The activity of Cr<sub>2</sub>O<sub>3</sub>/C-WI was enhanced compared with pure Cr<sub>2</sub>O<sub>3</sub>, while it was much lower than CrO<sub>x</sub>/C-450. This extraordinarily low temperature NH<sub>3</sub>-SCR performance makes CrO<sub>x</sub>/C-450 the best catalyst among all the samples derived from MIL-101. To evaluate the NH<sub>3</sub>-SCR performances on the catalysts more precisely, the normalized rates per mole transition metal were calculated and the results are displayed in Fig. 2a. The catalytic activity order is CrO<sub>x</sub>/C-450 > Mn<sub>2</sub>O<sub>3</sub> > Cr<sub>2</sub>O<sub>3</sub>/C-WI > Cr<sub>2</sub>O<sub>3</sub>. In addition, the apparent active energies of CrO<sub>x</sub>/C-450 and Cr<sub>2</sub>O<sub>3</sub> based catalysts were obtained when NO conversions were limited to low conversion (Fig. 2b and Table S2†). The apparent active energy of NH<sub>3</sub>-SCR on the CrO<sub>x</sub>/C-450 catalyst was lower than those of SCR on Cr<sub>2</sub>O<sub>3</sub>/C-WI and Cr<sub>2</sub>O<sub>3</sub>, which further confirms the superb catalytic activity of the CrO<sub>x</sub>/C-450 sample. Based on the kinetics data listed in Tables S3 and S4,† apparent kinetics equations of NH<sub>3</sub>-SCR on CrO<sub>x</sub>/C-450 and Cr<sub>2</sub>O<sub>3</sub>/C-WI catalysts were obtained (Fig. S2†). For CrO<sub>x</sub>/C-450,  $r = [\text{NH}_3]^{0.586}[\text{NO}]^{0.964}$  at 150 °C, while for Cr<sub>2</sub>O<sub>3</sub>/C-WI,  $r = [\text{NH}_3]^{0.433}[\text{NO}]^{0.092}$ . The different reaction rate equations of NH<sub>3</sub>-SCR on CrO<sub>x</sub>/C-450 and Cr<sub>2</sub>O<sub>3</sub>/C-WI catalysts indicated their different reaction mechanisms, which may result in different NH<sub>3</sub>-SCR performance of CrO<sub>x</sub>/C-450 and Cr<sub>2</sub>O<sub>3</sub>/C-WI catalysts. The N<sub>2</sub> selectivity of CrO<sub>x</sub>/C-450 remained at a high level (over 90%) in its operation temperature window, while those of Cr<sub>2</sub>O<sub>3</sub> and MnO<sub>2</sub> were very poor. This indicated that side reactions such as the formation of N<sub>2</sub>O hardly occurred on the CrO<sub>x</sub>/C-450 catalyst. SO<sub>2</sub>- and H<sub>2</sub>O-tolerance of CrO<sub>x</sub>/C-450 was further tested and the results are presented in Fig. 1c and S1c.† CrO<sub>x</sub>/C-450 exhibited over 80% NO conversion within 24 h in the presence of H<sub>2</sub>O, indicating its satisfactory water tolerance. When SO<sub>2</sub> was introduced into the feed gas, the activity of CrO<sub>x</sub>/C-450 gradually dropped to 60% within 20 h, while it dropped to 50% in 20 h when SO<sub>2</sub> and H<sub>2</sub>O co-existed in the feed gas. The activity of CrO<sub>x</sub>/C-450 could be recovered after a heat treatment at a temperature as low as 300 °C. This indicated that the poisoning effect of SO<sub>2</sub> on CrO<sub>x</sub>/C-450 could be accelerated by H<sub>2</sub>O, while H<sub>2</sub>O hardly influenced the regeneration ability of CrO<sub>x</sub>/C-450. In contrast, the MnO<sub>2</sub> catalyst



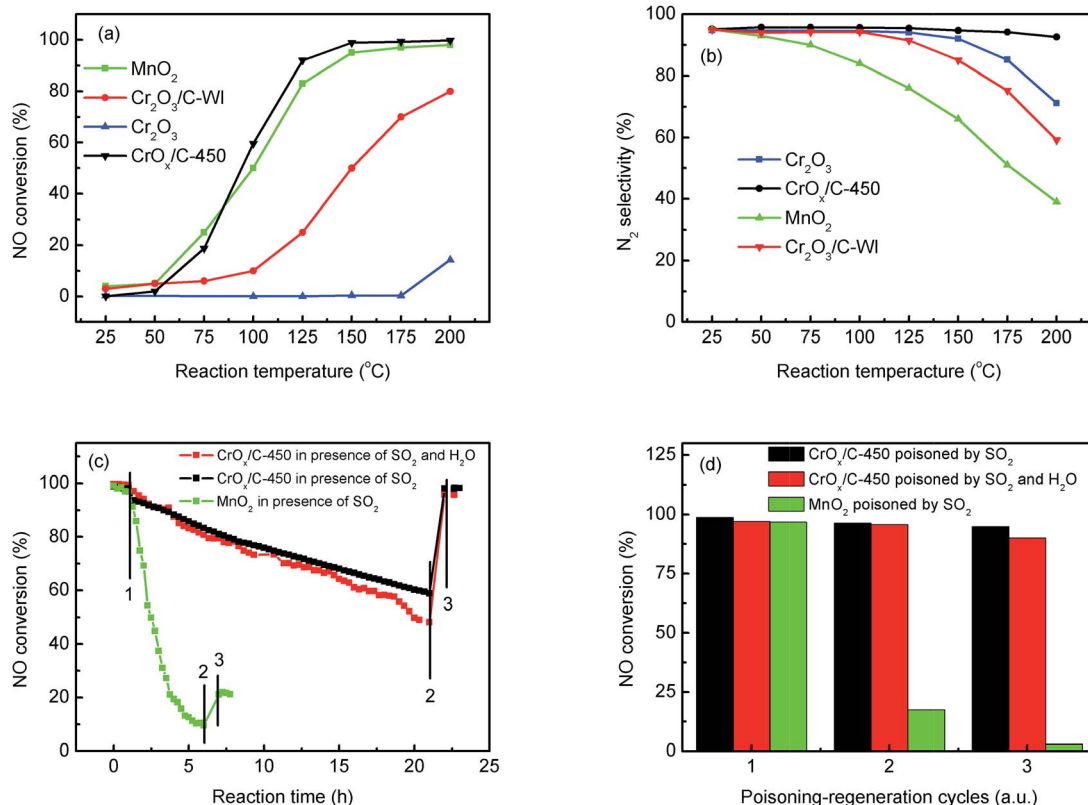


Fig. 1  $\text{NH}_3$ -SCR activity of catalysts: (a) NO conversion, (b)  $\text{N}_2$  selectivity, (c)  $\text{SO}_2$  poisoning test (step 1, 2, and 3 present  $\text{SO}_2$  and  $\text{H}_2\text{O}$  (when used) on,  $\text{SO}_2$  and  $\text{H}_2\text{O}$  (when used) off, and after regeneration), and (d) regeneration ability.

deactivated rapidly upon  $\text{SO}_2$  introduction in 6 h, and this process was irreversible. It was demonstrated that the  $\text{CrO}_x/\text{C-450}$  catalyst has satisfactory  $\text{SO}_2$ -tolerance. The regeneration ability of  $\text{CrO}_x/\text{C-450}$  was further studied. As shown in Fig. 1d, over 90% of the catalytic activity of  $\text{CrO}_x/\text{C-450}$  could be recovered as compared to that of the fresh catalyst after 3 poisoning-regeneration cycles irrespective of whether  $\text{H}_2\text{O}$  was introduced by regeneration at 300 °C in flowing  $\text{N}_2$ , while that of  $\text{MnO}_2$  catalyst dropped dramatically through only 1 poisoning-regeneration cycle, which indicated the remarkable regeneration ability of the  $\text{CrO}_x/\text{C-450}$  sample.

### 3.2. Structural information

To investigate the  $\text{NH}_3$ -SCR on the catalysts, the structural information of catalysts was necessary. XRD, XRF, FTIR, Raman, and TEM analyses were carried out to investigate the structural properties of the catalysts synthesized from MIL-101(Cr). The XRD patterns of all samples are shown in Fig. S3.† In the XRD pattern of the precursor, sharp and distinct peaks attributed to the MIL-101 phase were detected, which is in agreement with the data reported by Jhung *et al.*<sup>43</sup> When MIL-101 was heated in  $\text{N}_2$ -flow, the XRD peaks of MIL-101 became weak and gradually disappeared with an increase in

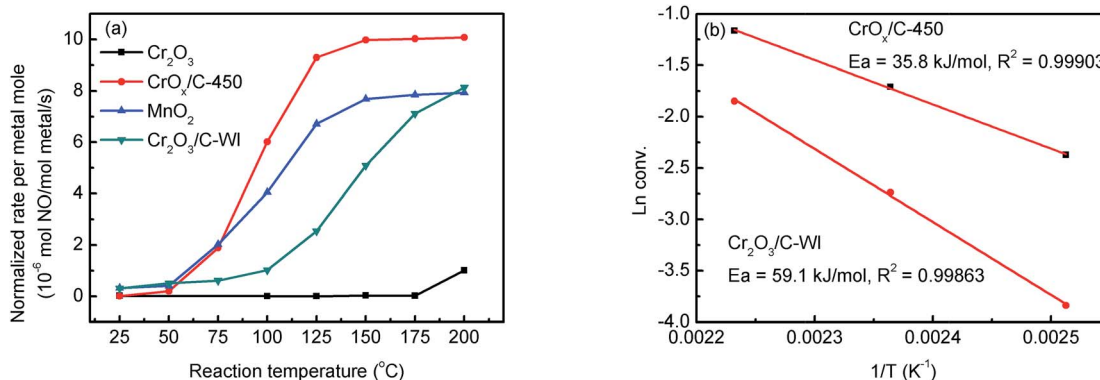


Fig. 2 (a) Normalized rates per metal mole of catalysts, (b) apparent active energy of  $\text{CrO}_x/\text{C-450}$  and  $\text{Cr}_2\text{O}_3/\text{C-WI}$  catalysts.

temperature. When the calcining temperature reached 450 °C, the peaks of the MIL-101 phase disappeared completely and replaced with wide and weak peaks at 24.5°, 33.5°, and 36.1°, which belonged to the (012), (104), and (110) plane, respectively, of the eskolaite phase (PDF#38-1479) as well as Cr<sub>2</sub>O<sub>3</sub>/C-WI.<sup>45</sup> This indicated that the MIL-101 structure could be destroyed through the calcining process, accompanied with the formation of the eskolaite phase. Furthermore, the CrO<sub>x</sub>/C-450 sample was found to have a small particle size based on its broad XRD peaks.

FTIR and Raman analyses were carried out to study the carbon species in the catalysts. As shown in Fig. S4a,<sup>†</sup> the bands at 3300 cm<sup>-1</sup>, 1600 cm<sup>-1</sup>, and 1400 cm<sup>-1</sup> were identified in the FTIR spectra of MIL-101. The broad band at 3300 cm<sup>-1</sup> arises due to the stretching vibration of the surface -OH groups. The two bands at 1600 and 1400 cm<sup>-1</sup> could be attributed to the stretching vibration of the -COO group of the organic linkers of MIL-101. However, the intensity of bands at 1600 cm<sup>-1</sup> and 1400 cm<sup>-1</sup> decreased on increasing the calcination temperature. This indicates that the organic linker begins to decompose and carbonize when the calcining temperature increases. The carbonization process was further investigated by Raman analysis (Fig. S4b<sup>†</sup>). Wide bands at 1360 and 1590 cm<sup>-1</sup>, corresponding to the D-band and G-band of MIL-101, were detected in the samples calcined at low temperatures, such as 350 and 400 °C. When the calcining temperature increased, the G-band gradually disappeared and the D-band still remained, which indicated the loss of the ordered structure of MOFs and the formation of amorphous carbon. In the spectrum of Cr-550, the G-band disappeared absolutely and only a wide D-band was observed. This illustrates that the organic linker carbonized and transformed to amorphous carbon during the calcining process, which accompanied with the destruction of the MOFs structure.

The elemental contents of catalysts were studied *via* XRF analysis. Since the organic species in MIL-101 completely transformed to amorphous carbon in CrO<sub>x</sub>/C-450, as mentioned before, the ignition loss in XRF analysis of CrO<sub>x</sub>/C-450 was believed to be the result of carbon species burning. Thus, the elemental contents of the catalysts could be calculated from the XRF data and the results are shown in Table 1. The CrO<sub>x</sub>/C-450 catalyst consisted of 19.2% Cr, 28.7% O, and 52.0% C. As it was designed, the elemental contents of Cr<sub>2</sub>O<sub>3</sub>/C-WI were similar to those of CrO<sub>x</sub>/C-450.

Table 1 Element contents and surface areas of catalysts

Sample	Contents <sup>a</sup> (wt%)		Elements contents (at%)			Surface area <sup>b</sup> (m <sup>2</sup> g <sup>-1</sup> catalyst)		
	Cr <sub>2</sub> O <sub>3</sub>	Ignition loss	Cr	O	C	Sample	Carbon support <sup>c</sup>	Active material
CrO <sub>x</sub> /C-450	70.2	29.8	19.2	28.7	52.0	256	784	20.8
Cr <sub>2</sub> O <sub>3</sub> /C-WI	69.5	30.5	18.9	28.4	52.7	279	897	9.9
Cr <sub>2</sub> O <sub>3</sub>	99.9	0.1	40.0	60.0	—	28	—	—

<sup>a</sup> Contents of catalysts were obtained from XRF analyses. <sup>b</sup> Surface areas of catalysts were obtained from N<sub>2</sub> adsorption/desorption analyses.

<sup>c</sup> Carbon support of CrO<sub>x</sub>/C-450 catalyst was obtained by washing CrO<sub>x</sub>/C-450 using hydrochloric acid. Carbon support of Cr<sub>2</sub>O<sub>3</sub>/C-WI is active carbon.

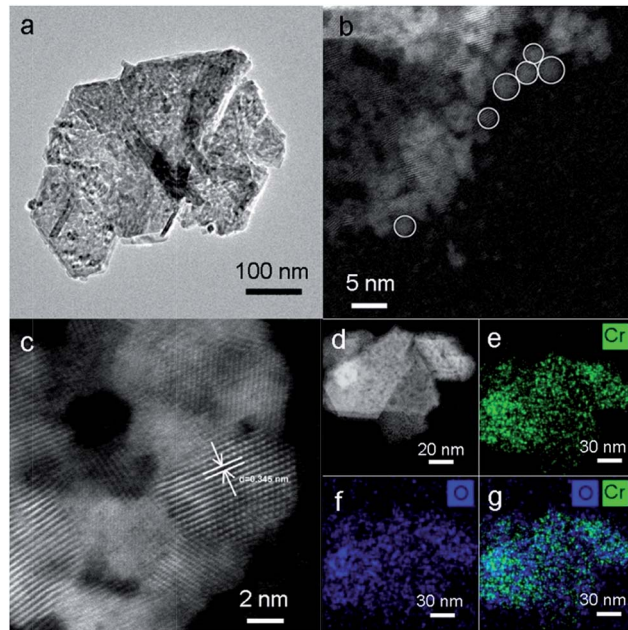


Fig. 3 (a) TEM image, (b–d) high resolution HAADF-STEM image of CrO<sub>x</sub>/C-450 catalyst. (e, f) 2D STEM EDS elemental maps of Cr K $\alpha$  (Green) and O (Blue) elements, respectively. (g) A superimposed image of (e) and (f).

TEM analysis was performed to investigate the structure of MIL-101, CrO<sub>x</sub>/C-450, and Cr<sub>2</sub>O<sub>3</sub>/C-WI. As shown in Fig. S5a,<sup>†</sup> the MIL-101 with octahedron morphology can be observed distinctly, while it transformed to a hexagonal sheet after calcination (Fig. 3a). Further structural information was obtained *via* high-angle annular dark field (HAADF) imaging (Fig. 3b). The hexagonal-like sample observed in Fig. 3a was actually an aggregation of nano-particles with an average size of 3 nm. In addition, lattice fringes of  $d = 0.345$  nm were observed (Fig. 3c), corresponding to the eskolaite Cr<sub>2</sub>O<sub>3</sub> (012) crystal plane, which further confirmed that the Cr oxide in the CrO<sub>x</sub>/C-450 catalyst has the eskolaite phase. From the EDX element mapping analysis (Fig. 3e–g), Cr element and O element were observed to be highly dispersed in the CrO<sub>x</sub>/C-450 sample and the superimposed image of Cr and O matches the HAADF image. It was estimated that the CrO<sub>x</sub>/C-450 catalyst was primarily formed by CrO<sub>x</sub> nano-particles with eskolaite phase as

designed in this study. The  $\text{CrO}_x/\text{C-450}$  sample after 3 poisoning-regeneration cycles was also imaged to investigate the stability of the catalyst (Fig. S5b†). The used sample was primarily composed of  $\text{CrO}_x$  nano-particles, similar to the fresh sample, and no major difference in the particle size of  $\text{Cr}_2\text{O}_3$  could be observed after 5 deactivation-regeneration circles, which evidently proved the stability of the sample  $\text{CrO}_x/\text{C-450}$ .  $\text{Cr}_2\text{O}_3$  and  $\text{Cr}_2\text{O}_3/\text{C-WI}$ , however, had a bulk-like shape (Fig. S5c and d†) with average particle sizes of over 100 nm. In the structure of the MIL-101 precursor, metal nodes containing 3 Cr atoms were covered by organic linkers. Therefore, it is reasonable to suggest that  $\text{CrO}_x$  nano-particles in the  $\text{CrO}_x/\text{C-450}$  catalyst stabilized by covering carbon species transformed from organic linkers of MIL-101 after the calcining process.

The feasible mechanism of catalyst synthesis is displayed in Fig. 4. During the calcination process, organic linkers covering Cr nodes carbonized and the structure of MIL-101 gradually destroyed. The amorphous carbon from organic linkers limited the growth of Cr nodes. Finally, when the calcined sample was exposed to air, the remaining Cr nano-particles were oxidized to  $\text{CrO}_x$  nano-particles with eskolaite phase, forming the structure of amorphous carbon covered  $\text{CrO}_x$  nano-particles ( $\text{CrO}_x/\text{C}$ ).

### 3.3. Textural properties of catalysts

As mentioned before, the  $\text{CrO}_x/\text{C-450}$  catalyst was primarily formed by  $\text{CrO}_x$  nano-particles with eskolaite phase and exhibited enhanced  $\text{NH}_3$ -SCR activity and satisfying regeneration ability. To explore the relationship between the structure of  $\text{CrO}_x/\text{C-450}$  and the  $\text{NH}_3$ -SCR performance, the properties of the catalysts were characterized by BET, XPS,  $\text{H}_2$ -TPR,  $\text{O}_2$ -TPD, and  $\text{NH}_3$ -TPD analyses.

The surface areas of the catalysts can influence the number of active sites on the catalyst surface, which is considered as an important fact affecting the catalytic activity of  $\text{NH}_3$ -SCR catalysts. The surface areas of  $\text{CrO}_x/\text{C-450}$ ,  $\text{Cr}_2\text{O}_3$ , and  $\text{Cr}_2\text{O}_3/\text{C-WI}$  obtained from BET analysis are listed in Table 1. The BET surface areas of  $\text{CrO}_x/\text{C-450}$  and  $\text{Cr}_2\text{O}_3/\text{C-WI}$  are similar and larger than that of  $\text{Cr}_2\text{O}_3$ . Due to the enhanced  $\text{NH}_3$ -SCR

performances of  $\text{CrO}_x/\text{C-450}$  and  $\text{Cr}_2\text{O}_3/\text{C-WI}$  (Fig. 1), it is believed that the enlarged surface area increased the activity of the Cr oxide catalyst. According to the reaction rates normalized by the surface areas of the active material of the catalysts,  $\text{CrO}_x/\text{C-450}$  exhibited comparatively superior NO conversion than  $\text{Cr}_2\text{O}_3/\text{C-WI}$  at 125 °C and 150 °C. This infers that a large surface area is not the only reason for the excellent  $\text{NH}_3$ -SCR activity of  $\text{CrO}_x/\text{C-450}$ .

The acidity of the catalysts, which can influence the absorption of reaction agents, is an important factor affecting the  $\text{NH}_3$ -SCR performance of catalysts. This property of catalysts was investigated by  $\text{NH}_3$ -TPD analysis. As displayed in Fig. S6a,† the  $\text{NH}_3$  desorption behaviours of  $\text{Cr}_2\text{O}_3$  and  $\text{CrO}_x/\text{C-450}$  were similar. No distinct  $\text{NH}_3$  desorption peak was observed from 150 to 400 °C in the profiles of both  $\text{Cr}_2\text{O}_3$  and  $\text{CrO}_x/\text{C-450}$  samples, which indicated the weak acidity of these two samples. Therefore, the giant  $\text{NH}_3$ -SCR performance difference between  $\text{Cr}_2\text{O}_3$  and  $\text{CrO}_x/\text{C}$  is not the result of acidity.

The redox ability of materials is another significant factor influencing the catalytic activity of the  $\text{NH}_3$ -SCR catalyst.  $\text{H}_2$ -TPR method was utilized to discuss this property of the synthesized catalysts. As illustrated in Fig. 5b,  $\text{Cr}_2\text{O}_3$  exhibited a single-peak profile. The  $\text{H}_2$  consumption peak at 343 °C was a result of one-step reduction from  $\text{Cr}^{6+}$  to  $\text{Cr}^{3+}$ , accompanied by the loss of lattice oxygen atoms connected with  $\text{Cr}^{6+}$  ions.<sup>46</sup> For

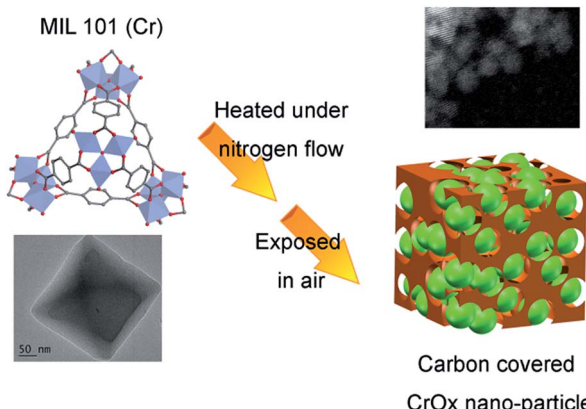


Fig. 4 Possible mechanism of catalyst synthesis (green spheres present  $\text{CrO}_x$  nano-particles, brown skolen present amorphous carbon).

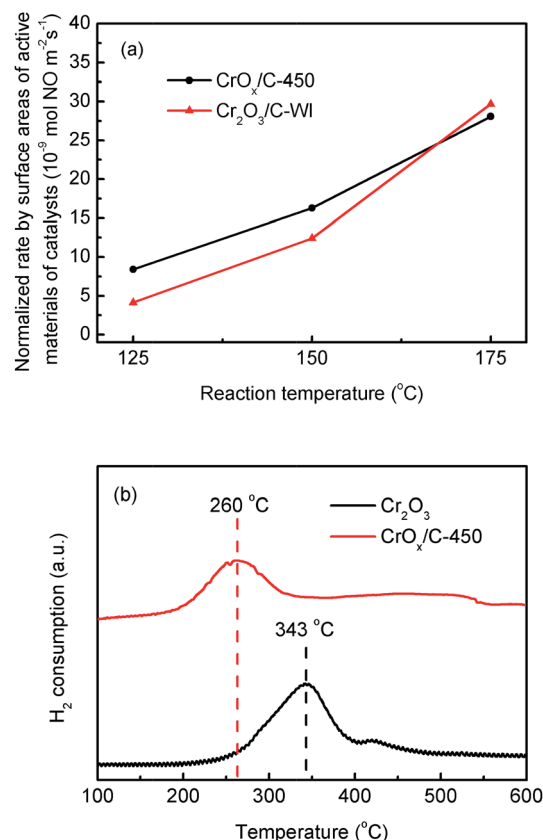


Fig. 5 (a) Normalized rates per surface areas of active material of  $\text{CrO}_x/\text{C-450}$  and  $\text{Cr}_2\text{O}_3/\text{C-WI}$  catalysts, (b)  $\text{H}_2$ -TPR result of  $\text{CrO}_x/\text{C-450}$  and bulk  $\text{Cr}_2\text{O}_3$ .



the  $\text{CrO}_x/\text{C}-450$  sample, the  $\text{H}_2$  consumption peak shifted to a low temperature, which indicated that  $\text{CrO}_x/\text{C}-450$  exhibited stronger oxidation ability and a higher amount of active lattice oxygen than  $\text{Cr}_2\text{O}_3$ . In addition,  $\text{O}_2$ -TPD analysis was carried out to investigate the stability of the oxygen atoms of the catalyst; the results are shown in Fig. S6b.† In the profile of  $\text{Cr}_2\text{O}_3$ , no  $\text{O}_2$  desorption peak was discovered in the temperature range from 50 °C to 450 °C, which indicates that the oxygen on the surface of  $\text{Cr}_2\text{O}_3$  is stable and inert. However, the curve of  $\text{CrO}_x/\text{C}-450$  exhibited an  $\text{O}_2$  desorption peak from 200 to 350 °C, which was much higher than the desorption temperature of absorbed  $\text{O}_2$  species recorded earlier.<sup>47</sup> Hence, the desorption peak from 200 to 350 °C was believed to correspond to the dissociation of lattice oxygen from  $\text{CrO}_x/\text{C}-450$ . This demonstrates that the lattice oxygen of  $\text{CrO}_x/\text{C}$  becomes more active and unstable than that of  $\text{Cr}_2\text{O}_3$ . Remarkably, the  $\text{CrO}_x/\text{C}$  catalyst has high surface atom/lattice atom rate for its ultrasmall size as mentioned before. It is reasonable to conclude that the unsaturated surface atoms of  $\text{CrO}_x/\text{C}$  cause the unique redox ability exhibited in  $\text{H}_2$ -TPR analysis and the instability of the lattice oxygen atom detected in  $\text{O}_2$ -TPD analysis. Unstable and activated oxygen atoms are inferred to enhance the activity of  $\text{CrO}_x/\text{C}$  catalyst.

In XPS analysis, Cr 2p spectra (Fig. 6a) of all the samples were comparable. The Cr 2p<sub>3/2</sub> peak could be divided into two peaks at 576.7 eV and 578.6 eV, belonging to  $\text{Cr}^{3+}$  and  $\text{Cr}^{6+}$ , respectively.<sup>48</sup> The relative contents of  $\text{Cr}^{3+}$  and  $\text{Cr}^{6+}$  ions were

analogous (Table 2), indicating their similar Cr state. The O 1s peak (Fig. 6b) could be separated into two peaks at 530.1 eV and 531.9 eV, attributed to the lattice oxygen and surface -OH groups, respectively.<sup>49,50</sup> The relative contents of these two types of oxygen species are also listed in Table 2. The  $\text{CrO}_x/\text{C}-450$  sample exhibited more surface -OH groups than  $\text{Cr}_2\text{O}_3$ . Notably, the peak belonging to the lattice oxygen of  $\text{CrO}_x/\text{C}-450$  shifts to the high binding energy side, contrasting with that of  $\text{Cr}_2\text{O}_3$  and  $\text{Cr}_2\text{O}_3/\text{C}-\text{WI}$ . It is evident that the lattice oxygen of  $\text{CrO}_x/\text{C}-450$  carries less negative charge than  $\text{Cr}_2\text{O}_3$  and  $\text{Cr}_2\text{O}_3/\text{C}-\text{WI}$ . Materials with an ultrasmall size are deemed to have abundant dangling bands and their surface atoms are usually unsaturated-coordinated. In case of  $\text{CrO}_x/\text{C}-450$ , some surface oxygen atoms are inferred to be unsaturated coordinated for ultrasmall size of  $\text{CrO}_x$  nano-particles. This unsaturated oxygen is considered to have less negative charge and is expected to be more active than the saturated coordinated oxygen of bulk  $\text{Cr}_2\text{O}_3$ .

Furthermore, to determine whether the lattice oxygen participates in the  $\text{NH}_3$ -SCR reaction, *ex situ* XPS analysis was carried out. The  $\text{CrO}_x/\text{C}-450$  catalyst was heated under  $\text{NH}_3 + \text{NO}$  flow at 150 °C for 1 h; the XPS spectra of  $\text{CrO}_x/\text{C}-450$  before and after treatment are displayed in Fig. 6c and d. In the Cr 2p spectra (Fig. 6c), the peak of  $\text{Cr}^{6+}$  at 578.6 eV disappeared after  $\text{NH}_3 + \text{NO}$  treatment, while the peak of  $\text{Cr}^{3+}$  at 576.7 eV enhanced. This infers that  $\text{Cr}^{6+}$  species on the surface of  $\text{CrO}_x/\text{C}$

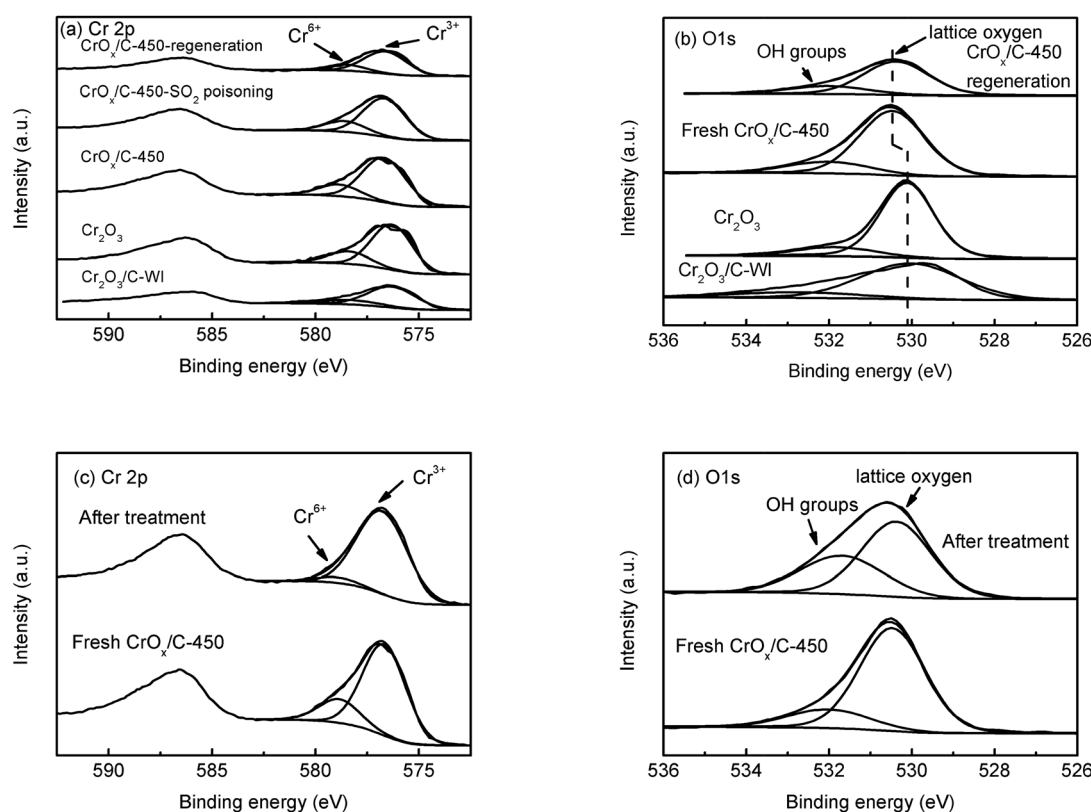


Fig. 6 XPS spectra of  $\text{Cr}_2\text{O}_3$ , fresh  $\text{CrO}_x/\text{C}-450$  catalyst,  $\text{SO}_2$  poisoned  $\text{CrO}_x/\text{C}-450$  catalyst, and regenerated  $\text{CrO}_x/\text{C}-450$  catalyst: (a) Cr 2p spectra, (b) O 1s spectra, and *ex situ* XPS analysis of fresh  $\text{CrO}_x/\text{C}-450$  catalyst and  $\text{CrO}_x/\text{C}-450$  catalyst heated under  $\text{NH}_3 + \text{NO}$  flow at 150 °C for 1 h: (c) Cr 2p spectra, (d) O 1s.

Table 2 Relative contents of Cr and O species on surfaces of catalysts

Sample	Cr 2p		O 1s	
	Cr <sup>3+a</sup> (%)	Cr <sup>6+a</sup> (%)	OH groups <sup>a</sup> (%)	Lattice oxygen <sup>a</sup> (%)
Cr <sub>2</sub> O <sub>3</sub>	76.74	23.26	13.39	86.61
CrO <sub>x</sub> /C-450	78.86	21.14	18.36	81.64
CrO <sub>x</sub> /C-450-regeneration	79.37	20.63	18.7	81.3
CrO <sub>x</sub> /C-450 <i>ex situ</i> treatment	94.87	5.13	36.76	63.24
CrO <sub>x</sub> /C-450-SO <sub>2</sub> poisoning	77.06	22.94	—	—

<sup>a</sup> Relative contents of Cr and O species were calculated from peak areas ratio of divided peaks in XPS spectra.

can react with the reagent molecules and eventually get consumed. Moreover, in the O 1s spectra (Fig. 6d), the peak intensity of lattice oxygen at 530.4 eV decreased after treatment, while the intensity of the peak attributed to the surface -OH group at 531.7 eV increased, which indicates the loss of surface lattice oxygen. Therefore, lattice oxygen was believed to take part in the NH<sub>3</sub>-SCR on the CrO<sub>x</sub>/C catalyst. Thus, CrO<sub>x</sub>/C-450, which has more active lattice oxygen, can exhibit enhanced NH<sub>3</sub>-SCR activity than Cr<sub>2</sub>O<sub>3</sub>.

### 3.4. Mechanism of NH<sub>3</sub>-SCR on CrO<sub>x</sub>/C catalyst

In "fast NH<sub>3</sub>-SCR", NO catalytically reduced NH<sub>3</sub> in assistance of NO<sub>2</sub>, which was reported to have lower activation energy and enhanced catalytic activity compared with the typical NH<sub>3</sub>-SCR. Herein, the CrO<sub>x</sub>/C catalyst was proved to have activated lattice oxygen. It is reasonable to deduce that NO can be oxidized to NO<sub>2</sub> by the activated oxygen on the CrO<sub>x</sub>/C surface, making the NH<sub>3</sub>-SCR on CrO<sub>x</sub>/C proceed as the "fast NH<sub>3</sub>-SCR" pathway. To verify this conjecture, NO oxidation on CrO<sub>x</sub>/C-450 and Cr<sub>2</sub>O<sub>3</sub>/C-WI catalysts was carried out. As displayed in Fig. 7a, NO could be oxidized to NO<sub>2</sub> on both CrO<sub>x</sub>/C-450 and Cr<sub>2</sub>O<sub>3</sub>/C-WI. However, the mass of formed NO<sub>2</sub> on CrO<sub>x</sub>/C-450 exceeded as compared to that on Cr<sub>2</sub>O<sub>3</sub>/C-WI. Moreover, the normalized rate by surface area of NO oxidation on CrO<sub>x</sub>/C-450 clearly surpassed that on Cr<sub>2</sub>O<sub>3</sub>/C-WI (Fig. 7b). This indicated that NO is more easily oxidized to NO<sub>2</sub> on CrO<sub>x</sub>/C-450 catalyst with activated oxygen, which probably resulted in the superb NH<sub>3</sub>-SCR performance of CrO<sub>x</sub>/C-450.

In order to confirm whether the formed NO<sub>2</sub> participated in NH<sub>3</sub>-SCR on the CrO<sub>x</sub>/C catalyst, further information about the reaction mechanism was obtained using DRIFTS. In the spectra of the absorption NO + O<sub>2</sub> saturated CrO<sub>x</sub>/C-450 sample (Fig. 8a), the bands centered at 1280, 1335, and 1520 cm<sup>-1</sup>, and a wide band divided into bands at 1730, 1690, and 1660 cm<sup>-1</sup> were detected. As reported elsewhere,<sup>51</sup> these IR bands were attributed to weakly bound NO<sub>2</sub> (1730 cm<sup>-1</sup>), nitrite anion (1335 cm<sup>-1</sup>),  $\nu_{\text{s}}(\text{N}=\text{O})$  and  $\nu_{\text{as}}(\text{N}=\text{O})$  of symmetric N<sub>2</sub>O<sub>3</sub> (1690 and 1660 cm<sup>-1</sup>), bidentate nitrates (1520 cm<sup>-1</sup>), and monodentate nitrates (1280 cm<sup>-1</sup>). When the feed gas was switched to NH<sub>3</sub>, the bands belonging to NO<sub>2</sub> and bidentate nitrates gradually disappeared, replacing with the bands of NH<sub>3</sub> absorbed on Lewis acid sites (1620 and 1217 cm<sup>-1</sup>),<sup>52,53</sup> while the bands corresponding to symmetric N<sub>2</sub>O<sub>3</sub>, nitrite anion, and monodentate nitrates were still present. Indeed, it is apparent that

NO<sub>2</sub> and bidentate nitrates participated in the surface reaction on CrO<sub>x</sub>/C-450 and were consumed by NH<sub>3</sub>, which is a typical "fast NH<sub>3</sub>-SCR" pathway.<sup>54</sup> To determine the role of NH<sub>3</sub>, co-absorption of NO + O<sub>2</sub> on CrO<sub>x</sub>/C-450 after pre-absorption of NH<sub>3</sub> was investigated (Fig. 8b). In the spectra of the absorption NH<sub>3</sub> saturated CrO<sub>x</sub>/C-450 sample, only a weak band at 1620 cm<sup>-1</sup> corresponding to NH<sub>3</sub> on Lewis acid sites was detected, indicating the low acidity of CrO<sub>x</sub>/C-450 as mentioned in NH<sub>3</sub>-TPD analysis. With the addition of NO and O<sub>2</sub>, this band gradually disappeared, accompanied by the appearance of bands belonging to weakly bound NO<sub>2</sub> (1732 cm<sup>-1</sup>), nitrite anion (1333 cm<sup>-1</sup>),  $\nu_{\text{s}}(\text{N}=\text{O})$  and  $\nu_{\text{as}}(\text{N}=\text{O})$  of symmetric N<sub>2</sub>O<sub>3</sub> (1691 and 1657 cm<sup>-1</sup>), and bidentate nitrates (1515 cm<sup>-1</sup>).<sup>51</sup>

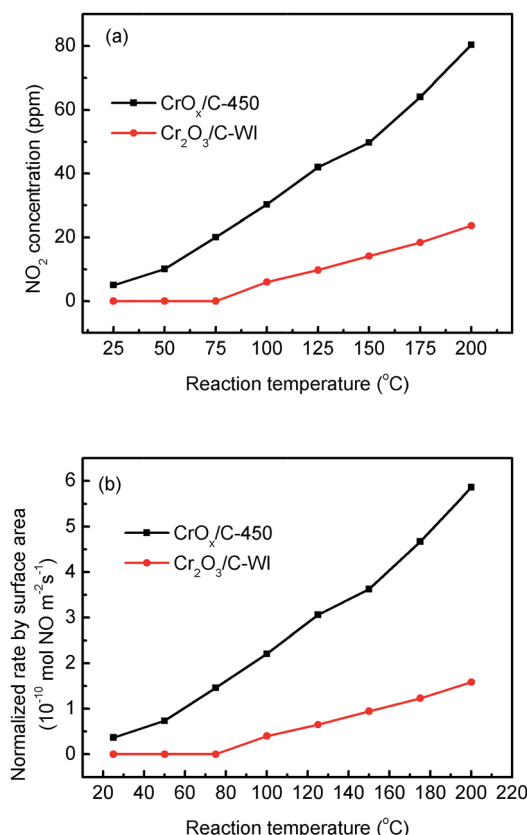


Fig. 7 (a) NO oxidation performances and (b) normalized NO oxidation rate by surface area on CrO<sub>x</sub>/C-450 and Cr<sub>2</sub>O<sub>3</sub>/C-WI catalysts.



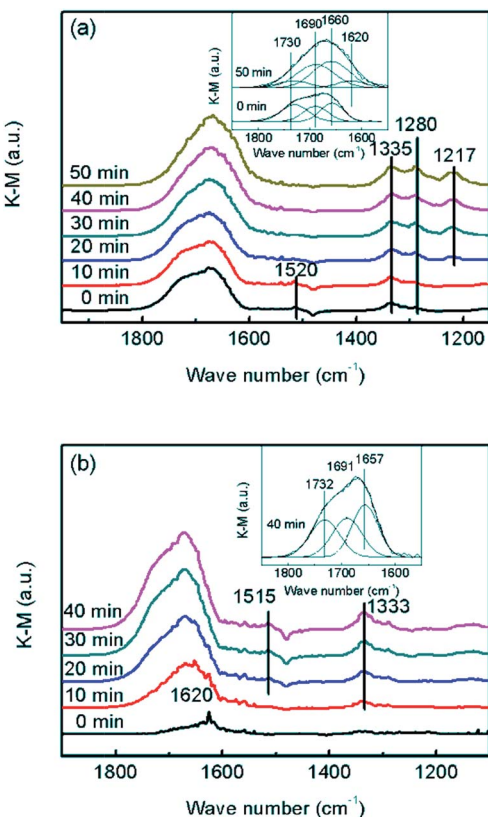


Fig. 8 *In situ* DRIFT spectra of  $\text{CrO}_x/\text{C-450}$ : (a)  $\text{NH}_3$  reacted with pre-absorbed  $\text{NO} + \text{O}_2$ , (b)  $\text{NO} + \text{O}_2$  reacted with pre-absorbed  $\text{NH}_3$ .

This indicated that  $\text{NH}_3$  on Lewis sites was reacted and consumed. Therefore, the entire  $\text{NH}_3$ -SCR on  $\text{CrO}_x/\text{C-450}$  followed a L-H mechanism, in which  $\text{NO}$  was oxidized by the unsaturated oxygen of  $\text{CrO}_x/\text{C-450}$  catalyst and transformed to  $\text{NO}_2$ . The formed  $\text{NO}_2$  further absorbed on the surface of  $\text{CrO}_x/\text{C-450}$  as bidentate nitrates, and reacted with  $\text{NH}_3$  on Lewis sites, forming  $\text{N}_2$  and  $\text{H}_2\text{O}$  at last. Due to the formation of  $\text{NO}_2$ , the reaction proceeded as a “fast  $\text{NH}_3$ -SCR” pathway, causing the decrease in reaction activation energy, thus enhancing the low-temperature activity.

### 3.5. Reasons of excellent $\text{SO}_2$ tolerance of regeneration ability

Sulfation process is a transition from metal oxide to metal sulfate. Irrespective of which type of intermediate exists in the sulfation process, the metal–oxygen band must be broken. It is reasonable to deduce that a metal oxide with a strong metal–oxygen band is difficult to be sulfated. The Cr–O band energy of the eskolaite phase  $\text{Cr}_2\text{O}_3$  was calculated (see the ESI†). As displayed in Table S5,† the band energy of the Cr–O band in the eskolaite phase  $\text{Cr}_2\text{O}_3$  exceeds that of Mn–O band in  $\text{MnO}_2$ , indicating that the sulfation process of  $\text{Cr}_2\text{O}_3$  proceeds with more difficulty as compare that of  $\text{MnO}_2$ . This is considered to be the result of the various  $\text{NH}_3$ -SCR performances of  $\text{MnO}_2$  and  $\text{CrO}_x/\text{C-450}$  catalyst in the presence of  $\text{SO}_2$ . Moreover,  $\text{MnO}_2$  and  $\text{CrO}_x/\text{C-450}$  catalysts deactivated by  $\text{SO}_2$  were washed with

deionized water and the metal-ion contents in the eluate were measured by ICP analysis. As presented in Table S6,†  $\text{Mn}^{2+}$  was detected in the eluate of the deactivated  $\text{MnO}_2$  sample, while no  $\text{Cr}^{3+}$  was detected in the eluate of the deactivated  $\text{CrO}_x/\text{C-450}$  sample. It is evident that the  $\text{CrO}_x/\text{C-450}$  sample was protected from sulfation.

To further understand the  $\text{SO}_2$  poisoning and regeneration processes, the XPS spectra of the fresh  $\text{CrO}_x/\text{C-450}$  catalyst,  $\text{SO}_2$ -poisoned sample, and regenerated sample were studied. As displayed in Fig. 6a and Table 2, the Cr state and relative content of  $\text{Cr}^{6+}$  and  $\text{Cr}^{3+}$  of each sample were similar, which indicated that, as it is designed,  $\text{CrO}_x/\text{C-450}$  catalyst was difficult to be sulfated for the high lattice energy of  $\text{Cr}_2\text{O}_3$ . Comparing the O 1s peak of the fresh  $\text{CrO}_x/\text{C-450}$  sample and the regenerated sample (Fig. 6b), their peaks of lattice oxygen were similar and both shifted to the high binding energy side than that of bulk  $\text{Cr}_2\text{O}_3$ . Since activated lattice oxygen still remained on the surface, the regenerated catalyst exhibited high  $\text{NH}_3$ -SCR activity, similar to the fresh catalyst.

In XPS spectra of the  $\text{SO}_2$  poisoned sample, the peaks of S 2p and N 1s were detected. The S 2p peak (Fig. S7a†) consists of two peaks at 168.5 eV ( $\text{S } 2\text{p}_{1/2}$ ) and 169.7 eV ( $\text{S } 2\text{p}_{3/2}$ ), which belonged to  $\text{SO}_4^{2-}$ . The N 1s spectra (Fig. S7b†) can be divided into two peaks at 399.5 eV and 400.5 eV, contributed to  $\text{NH}_3$  and  $\text{NH}_4^+$ , respectively. According to the relative atom contents listed in Table S7,† atoms-ratio of  $\text{SO}_4^{2-}$  and  $\text{NH}_4^+$  was nearly 1 : 1 on the surface of the  $\text{SO}_2$ -poisoned sample. This indicated that  $\text{NH}_4\text{HSO}_4$  deposited on the surface of  $\text{CrO}_x/\text{C-450}$  during the  $\text{SO}_2$  poisoning process, which causes the deactivation of the catalyst. After heat treatment, the deposited  $\text{NH}_4\text{HSO}_4$  could easily decompose and the  $\text{CrO}_x/\text{C-450}$  catalyst with exposed activated lattice oxygen regains the superior activity.

## 4. Conclusions

In this study, we successfully designed and synthesized a novel chromium oxide nano-particles catalyst with excellent  $\text{NH}_3$ -SCR activity at 150 °C and remarkable  $\text{SO}_2$  regenerative ability. The obtained  $\text{CrO}_x/\text{C-450}$  catalyst was composed of  $\text{CrO}_x$  nano-particles covered by amorphous carbon. A carbon species, which was derived from the organic linkers of the MOFs precursor, protected the  $\text{CrO}_x$  nano-particles from aggregation.  $\text{CrO}_x/\text{C}$  catalysts primarily have Eskolaite phase  $\text{Cr}_2\text{O}_3$  with average size of 3 nm and exhibit a large surface area. Due to the small size of  $\text{CrO}_x$  nano-particles in  $\text{CrO}_x/\text{C}$  catalysts, the lattice oxygen atoms of  $\text{CrO}_x/\text{C}$  were activated, so that  $\text{NO}$  could be oxidized to  $\text{NO}_2$  on the catalyst surface. The formed  $\text{NO}_2$  participated in reaction and made  $\text{NH}_3$ -SCR on  $\text{CrO}_x/\text{C}$  proceed through a “fast  $\text{NH}_3$ -SCR” pathway. The large surface area and activated lattice oxygen of  $\text{CrO}_x/\text{C}$  catalysts caused the enhanced  $\text{NH}_3$ -SCR activities. Due to the stable lattice of  $\text{Cr}_2\text{O}_3$ ,  $\text{CrO}_x/\text{C}$  catalyst could hardly be sulfated in the  $\text{SO}_2$  poisoning process. Therefore, the regenerated catalyst still retained prominent activity when  $\text{NH}_4\text{HSO}_4$  deposited on the surface of the catalyst was removed during the regeneration process.



## Conflicts of interest

There are no conflicts to declare.

## Acknowledgements

The financial supports of National High-tech Research and Development (863) Program of China (2015AA03A401), National Natural Science Foundation of China (No. 21573105), Natural Science Foundation of Jiangsu Province (BK20161392), and Jiangsu Province Science and Technology Support Program (Industrial, BE2014130) are gratefully acknowledged.

## References

- 1 C. Liu, J. W. Shi, C. Gao and C. M. Niu, *Appl. Catal., A*, 2016, **522**, 54–69.
- 2 T. H. Vuong, J. Radnik, E. Kondratenko, M. Schneider, U. Armbruster and A. Bruckner, *Appl. Catal., B*, 2016, **197**, 159–167.
- 3 T. H. Vuong, J. Radnik, M. Schneider, H. Atia, U. Armbruster and A. Bruckner, *Catal. Commun.*, 2016, **84**, 171–174.
- 4 C. J. Tang, H. L. Zhang and L. Dong, *Catal. Sci. Technol.*, 2016, **6**, 1248–1264.
- 5 S. Wu, X. Yao, L. Zhang, Y. Cao, W. Zou, L. Li, K. Ma, C. Tang, F. Gao and L. Dong, *Chem. Commun.*, 2015, **51**, 3470–3473.
- 6 K. Wijayanti, S. Andonova, A. Kumar, J. Li, K. Kamasamudram, N. W. Currier, A. Yezerets and L. Olsson, *Appl. Catal., B*, 2015, **166**, 568–579.
- 7 J. H. Lee, Y. J. Kim, T. Ryu, P. S. Kim, C. H. Kim and S. B. Hong, *Appl. Catal., B*, 2017, **200**, 428–438.
- 8 P. Chen, R. Moos and U. Simon, *J. Phys. Chem. C*, 2016, **120**, 25361–25370.
- 9 J. Liu, X. Li, Q. Zhao, J. Ke, H. Xiao, X. Lv, S. Liu, M. Tade and S. Wang, *Appl. Catal., B*, 2017, **200**, 297–308.
- 10 T. Boningari, P. R. Ettireddy, A. Somogyvari, Y. Liu, A. Vorontsov, C. A. McDonald and P. G. Smirniotis, *J. Catal.*, 2015, **325**, 145–155.
- 11 H. Hu, S. X. Cai, H. R. Li, L. Huang, L. Y. Shi and D. S. Zhang, *ACS Catal.*, 2015, **5**, 6069–6077.
- 12 Z. M. Liu, J. Z. Zhu, J. H. Li, L. L. Ma and S. I. Woo, *ACS Appl. Mater. Interfaces*, 2014, **6**, 14500–14508.
- 13 H. Chang, X. Chen, J. Li, L. Ma, C. Wang, C. Liu, J. W. Schwank and J. Hao, *Environ. Sci. Technol.*, 2013, **47**, 5294–5301.
- 14 J. Li, H. Chang, L. Ma, J. Hao and R. T. Yang, *Catal. Today*, 2011, **175**, 147–156.
- 15 C. Liu, L. Chen, J. Li, L. Ma, H. Arandiyan, Y. Du, J. Xu and J. Hao, *Environ. Sci. Technol.*, 2012, **46**, 6182–6189.
- 16 L. Zhang, L. L. Li, Y. Cao, X. J. Yao, C. Y. Ge, F. Gao, Y. Deng, C. J. Tang and L. Dong, *Appl. Catal., B*, 2015, **165**, 589–598.
- 17 D. W. Kwon, K. B. Nam and S. C. Hong, *Appl. Catal., B*, 2015, **166**, 37–44.
- 18 G. Qi and R. T. Yang, *Appl. Catal., B*, 2003, **44**, 217–225.
- 19 C. Liu, J.-W. Shi, C. Gao and C. Niu, *Appl. Catal., A*, 2016, **522**, 54–69.
- 20 M. Colombo, I. Nova, E. Tronconi, V. Schmeißer, B. Bandl-Konrad and L. Zimmermann, *Appl. Catal., B*, 2012, **111–112**, 106–118.
- 21 S. Roy, M. S. Hegde and G. Madras, *Appl. Energy*, 2009, **86**, 2283–2297.
- 22 B. Guan, R. Zhan, H. Lin and Z. Huang, *Appl. Therm. Eng.*, 2014, **66**, 395–414.
- 23 S. X. Cai, H. Hu, H. R. Li, L. Y. Shi and D. S. Zhang, *Nanoscale*, 2016, **8**, 3588–3598.
- 24 E. Rhodes and A. R. Ubbelohde, *Proc. R. Soc. A*, 1959, **251**, 156–171.
- 25 M. Kang, E. D. Park, J. M. Kim and J. E. Yie, *Catal. Today*, 2006, **111**, 236–241.
- 26 A. Zhou, D. Yu, L. Yang and Z. Sheng, *Appl. Surf. Sci.*, 2016, **378**, 167–173.
- 27 S. Xiong, X. Xiao, N. Huang, H. Dang, Y. Liao, S. Zou and S. Yang, *Environ. Sci. Technol.*, 2017, **51**, 531–539.
- 28 Q.-l. Chen, R.-t. Guo, Q.-s. Wang, W.-g. Pan, W.-h. Wang, N.-z. Yang, C.-z. Lu and S.-x. Wang, *Fuel*, 2016, **181**, 852–858.
- 29 H. E. Curry-Hyde, H. Musch and A. Baiker, *Appl. Catal.*, 1990, **65**, 211–223.
- 30 B. L. Duffy, H. E. Curry-Hyde, N. W. Cant and P. F. Nelson, *J. Catal.*, 1994, **149**, 11–22.
- 31 G. Busca, L. Lietti, G. Ramis and F. Berti, *Appl. Catal., B*, 1998, **18**, 1–36.
- 32 G. Marban, R. Antuna and A. B. Fuertes, *Appl. Catal., B*, 2003, **41**, 323–338.
- 33 E. Curry-Hyde and A. Baiker, *Ind. Eng. Chem. Res.*, 1990, **29**, 1985–1989.
- 34 S. Alayoglu, A. U. Nilekar, M. Mavrikakis and B. Eichhorn, *Nat. Mater.*, 2008, **7**, 333–338.
- 35 K. Yamamoto, T. Imaoka, W. J. Chun, O. Enoki, H. Katoh, M. Takenaga and A. Sonoi, *Nat. Chem.*, 2009, **1**, 397–402.
- 36 C. T. Campbell and Z. Mao, *ACS Catal.*, 2017, **7**, 8460–8466.
- 37 K. Shen, X. Chen, J. Chen and Y. Li, *ACS Catal.*, 2016, **6**, 5887–5903.
- 38 P. Yin, T. Yao, Y. Wu, L. Zheng, Y. Lin, W. Liu, H. Ju, J. Zhu, X. Hong, Z. Deng, G. Zhou, S. Wei and Y. Li, *Angew. Chem., Int. Ed. Engl.*, 2016, **55**, 10800–10805.
- 39 P. Mahata, D. Sarma, C. Madhu, A. Sundaresen and S. Natarajan, *Dalton Trans.*, 2011, **40**, 1952–1960.
- 40 P. Yin, T. Yao, Y. Wu, L. Zheng, Y. Lin, W. Liu, H. Ju, J. Zhu, X. Hong, Z. Deng, G. Zhou, S. Wei and Y. Li, *Angew. Chem., Int. Ed.*, 2016, **55**, 10800–10805.
- 41 B. You, N. Jiang, M. Sheng, W. S. Drisdell, J. Yano and Y. Sun, *ACS Catal.*, 2015, **5**, 7068–7076.
- 42 J. Yu, F. Guo, Y. Wang, J. Zhu, Y. Liu, F. Su, S. Gao and G. Xu, *Appl. Catal., B*, 2010, **95**, 160–168.
- 43 S. H. Jhung, J. H. Lee, J. W. Yoon, C. Serre, G. Ferey and J. S. Chang, *Adv. Mater.*, 2007, **19**, 121–124.
- 44 A. Henschel, K. Gedrich, R. Krahnert and S. Kaskel, *Chem. Commun.*, 2008, 4192–4194.
- 45 O. Kouvo and Y. Vuorelainen, *Am. Mineral.*, 1958, **43**, 1098–1106.
- 46 F. Ayari, M. Mhamdi, D. P. Debecker, E. M. Gaigneaux, J. Alvarez-Rodriguez, A. Guerrero-Ruiz, G. Delahay and A. Ghorbel, *J. Mol. Catal. A: Chem.*, 2011, **339**, 8–16.



47 M. A. Henderson and M. H. Engelhard, *J. Phys. Chem. B*, 2014, **118**, 29058–29067.

48 B. Wichterlova, L. Krajcikova, Z. Tvaruzkova and S. Beran, *J. Chem. Soc., Faraday Trans. 1*, 1984, **80**, 2639–2645.

49 D. Shuttleworth, *J. Phys. Chem.*, 1980, **84**, 1629–1634.

50 T. Dickinson, A. F. Povey and P. M. A. Sherwood, *J. Chem. Soc., Faraday Trans.*, 1976, **72**, 686–705.

51 K. I. Hadjiivanov, *Catal. Rev.*, 2000, **42**, 71–144.

52 X. Li, X. Li, J. Li and J. Hao, *J. Hazard. Mater.*, 2016, **318**, 615–622.

53 Z. Liu, S. Zhang, J. Li and L. Ma, *Appl. Catal., B*, 2014, **144**, 90–95.

54 Y. An, Y. Liu, P. An, J. Dong, B. Xu, Y. Dai, X. Qin, X. Zhang, M.-H. Whangbo and B. Huang, *Angew. Chem., Int. Ed. Engl.*, 2017, **56**, 3036–3040.

